

1 **Source of the 6 February 2013 Mw 8.0 Santa Cruz Islands**
2 **Tsunami**

3
4

5 **F. Romano¹, I. Molinari¹, S. Lorito¹, and A. Piatanesi¹**

6
7 ¹Istituto Nazionale di Geofisica e Vulcanologia, Via di Vigna Murata 605, 00143, Rome,
8 Italy

9
10 Corresponding author: Fabrizio Romano (*fabrizio.romano@ingv.it*)

11
12
13 *February 2015, Submission to NHESS (special issue “Progress in tsunami science in light*
14 *of the 2004 and 2011 tsunamis”)*

15
16
17 *Revised on May 2015*

18 **Abstract**

19 On 6 February 2013 an M_w 8.0 subduction earthquake occurred close to Santa Cruz Islands
20 at the transition between the Solomon and the New Hebrides Trench. The ensuing tsunami
21 caused significant inundation on the closest Nendo Island. The seismic source was studied
22 with teleseismic broadband P waves inversion optimized with tsunami forward modeling at
23 DART buoys (Lay et al., 2013), and with inversion of teleseismic body and surface waves
24 (Hayes et al., 2014). The two studies also use different hypocenters and different planar fault
25 models, and found quite different slip models. In particular, Hayes et al. (2014) argued for
26 an aseismic slip patch SE from the hypocenter. We here develop a 3D model of the fault
27 surface from seismicity analysis and retrieve the tsunami source by inverting DART and
28 tide-gauge data. Our tsunami source model features a main slip patch (peak value of ~ 11 m)
29 SE of the hypocentre, and reaching the trench. The rake direction is consistent with the
30 progressively more oblique plate convergence towards the Solomon trench. The tsunami
31 source partially overlaps the hypothesized aseismic slip area, which then might have slipped
32 coseismically.

33

34 **1 Introduction**

35 On 6 February 2013 an M_w 8.0 earthquake occurred in the Pacific Ocean nearby the
36 archipelago of Santa Cruz Islands. The hypocenter (165.138°E 10.738°S, depth ~29 km,
37 USGS, <http://earthquake.usgs.gov/earthquakes/eqarchives/poster/2013/20130205.php>) is
38 located at the subduction interface between the Australia and the Pacific plates, 76 km West
39 from Lata, the main city of Nendo Island (Fig. 1 and Fig. 2).

40 This earthquake, the largest in 2013, occurred on a complex section of the Australia-Pacific
41 plate boundary at the northern end of the New Hebrides trench (Hayes et al., 2012), nearby a
42 short segment of dominantly strike-slip plate motion that marks the transition between
43 Vanuatu and the Solomon Islands subduction zones. This segment is characterized by a
44 complex tectonic regime that becomes progressively more oblique westward as revealed by
45 the focal mechanisms of the local seismicity (Fig. 1). In this region the relative convergence
46 velocity between Australia and Pacific plates is ~9.4 cm/yr (DeMets et al., 2010).

47 The Santa Cruz Islands earthquake generated a tsunami that struck the Nendo Island, in
48 particular the city of Lata with waves higher than 1 m. Several runup and flowdepth
49 measurements have been collected during a field survey conducted on some islands of the
50 archipelago a few days after the earthquake (Fritz et al., 2014), reporting maximum tsunami
51 wave heights of about 11 m in the western part of the Nendo Island. In addition, the tsunami
52 propagated in the Pacific Ocean, also reaching the coasts of Hawaii (Lay et al., 2013).

53 Seismic and tsunami source of this earthquake have been previously studied with different
54 methodologies (Lay et al., 2013; Hayes et al., 2014a), highlighting some differences
55 between the resulting models in terms of both slip patch positions and slip amplitude. Hayes
56 et al. (2014a) studied the Santa Cruz Islands earthquake by inverting teleseismic body and
57 surface waves; Lay et al. (2013) performed a teleseismic broadband P wave inversion
58 optimized with tsunami forward modelling at DART buoys. These studies used different
59 hypocenters and different planar fault models; in particular, Lay et al. (2013) adopted both
60 hypocenter and fault plane shallower than those used by Hayes et al. (2014a). The best-
61 fitting source model in Hayes et al. (2014a, hereinafter HA14) has a main patch of slip
62 centred around the hypocenter with a maximum slip of about 4 m and a second smaller patch
63 located SE of the Nendo Island and characterized by relatively low slip (~0.5 m). On the
64 other hand, the source model in Lay et al. (2013, hereinafter LA13) features two patches
65 with slip larger than 10 m; the first patch is located around the hypocenter, whereas the
66 second one is shallower and located SE of the hypocenter. The surface projection of the slip
67 in LA13 is roughly consistent with the HA14 patches even though they are at different

68 depths (and featuring quite different slip values), because of the different fault planes used.
69 In addition, the LA13 source model is more efficient in terms of tsunami wave excitation
70 than that of HA14 and quite well predicts the tsunami observations recorded at the DART
71 buoys.

72 The usual pattern of the aftershocks distribution following a great subduction earthquake
73 should show a large number of events occurring along the unbroken portion of the
74 subduction interface, eventually also bordering the broken asperities (Aki, 1979). On the
75 other hand, as already extensively discussed (Hayes et al., 2014a; Lay et al., 2013), after the
76 6 February 2013 event, very few events were located along the subduction interface.
77 Furthermore, most of early aftershocks in the epicentral area (~200 events within 48 hours
78 from the mainshock, <http://earthquake.usgs.gov/earthquakes/?source=sitenav>) showed
79 strike-slip and normal mechanism, including two earthquakes with $M_w > 7$ occurred in the
80 upper crust portion of the Pacific plate and in the outer-rise trench region. HA14 proposed a
81 block-like motion behaviour of the Pacific upper plate to explain these observations. In
82 particular, they argued that a large number of anomalous right-lateral strike-slip events
83 located southeast of Nendo Island were triggered by significant aseismic slip along a portion
84 of the megathrust south-eastward from the epicentral area. However, LA13 model features
85 significant coseismic slip on this portion of the fault; these differences may be due to the
86 different data used and/or to the different fault models adopted in the inversions.

87 Here we study the coseismic tsunami source of the Santa Cruz Islands earthquake by
88 inverting the available tsunami waveforms. We compute the Green's functions at the DART
89 buoys and tide gauges using a 3D fault model that honours the complex geometry of the
90 subduction interface. After retrieving the tsunami source model, we discuss it in comparison
91 with LA13 and HA14 source models.

92
93

94 **2 Tsunami Data and Fault model**

95 The tsunami generated by the Santa Cruz Islands earthquake propagated both in the North
96 and South Pacific Ocean and it has been observed in the open sea at several DART buoys
97 and at some tide gauges located along the coasts of Solomon and Fiji Islands. We select 5
98 DART buoys (52403, 52406, 51425, 55012, and 55023,
99 <http://www.ndbc.noaa.gov/dart.shtml>) and 3 tide gauges (Lata Wharf, Honiara, and Lautoka,
100 <http://www.ioc-sealevelmonitoring.org>) that distinctly recorded a tsunami signal and that
101 allow a good azimuthal coverage (Fig. 2, further details in Supplementary Material). Before

102 using the tsunami data in the inversion, we remove the tide from the original signals by
103 using a robust LOWESS procedure (Barbosa et al., 2004).

104 The fault model geometry can greatly influence the results of source inversion. Adopting a
105 fault geometry that honours the complexities of the subduction interface then may help to
106 reduce the epistemic uncertainties associated to forward modelling (Romano et al., 2014).
107 This is particularly true for earthquakes of this size occurring in subduction zones
108 characterized by strong variations of strike and/or dip (e.g. Hayes et al., 2014b), even more
109 so in complex tectonic environments like the Santa Cruz Islands region.

110 Thus, analysing the aftershocks distribution occurred after the 6 February mainshock, the
111 local seismicity, and considering the rupture area expected for a M8 event, we built a 3D
112 non-planar fault model with variable strike and dip angles in order to account for such
113 geometrical complexities of the subduction interface on both the New Hebrides and
114 Solomon trenches (Bird, 2003). In particular, we selected from the EHB global relocation
115 earthquake catalogue (<http://www.isc.ac.uk/ehbulletin/>; Engdahl et al., 1998) the events
116 occurred in the area covered by the aftershocks of the Santa Cruz Islands earthquake and
117 having $M > 4.5$. After removing those ones relatively distant from the trench (distance > 200
118 km), we drew sections perpendicular to the trench at a distance of ~ 20 km each (measured
119 along the trench) projecting on them all the events in a neighbourhood of 30 km. We
120 obtained several 2D profiles by fitting the data of each section. The resulting suite of 2D
121 profiles was then further interpolated using CUBIT software (<http://cubit.sandia.gov>) in
122 order to obtain a 3D fault model, meshed into 45 quadrangular patches (9 along strike and 5
123 along dip, Figs. 2, S1, S2) with an average size of about 20 x 20 km. Our final fault model is
124 consistent with the northern interface of Vanuatu slab model in Slab1.0 (Hayes et al., 2012,
125 <http://earthquake.usgs.gov/data/slab/>) and extends both up to the trench and in the north-
126 west direction for ~ 40 -60 km. The dimensions of the resulting fault are ~ 180 km along strike
127 and ~ 90 km along dip (see Figs. 2, S1, S2).

128

129

130 **3 Green's functions and Inversion scheme**

131 The tsunami Green's functions are computed by means of NEOWAVE, a nonlinear
132 dispersive model for tsunami waves propagation (Yamazaki et al., 2009; Yamazaki et al.,
133 2011). The initial conditions for tsunami propagation are analytically computed (further
134 details in Meade, 2007; Romano et al., 2012) and they also include the contribution of the

135 coseismic horizontal deformation in the region of steep bathymetric slopes (Tanioka and
136 Satake, 1996).

137 For tsunami modelling at the DART buoys we use a bathymetric grid with a spatial
138 resolution of 1 arc-min, whereas the Green's functions at the tide gauges are computed on a
139 grid of 30 arc-sec in order to better model the nearshore tsunami propagation. The
140 bathymetric data set used for tsunami simulations is SRTM30+
141 (http://topex.ucsd.edu/WWW_html/srtm30_plus.html), which is resampled for the grid of 1
142 arc-min.

143 We solve the inverse problem by using the Heat Bath algorithm, which is a particular
144 implementation of the Simulated Annealing technique (Rothman, 1986). For tsunami
145 waveforms we use a cost function that is sensitive both to amplitude and phase matching
146 (Spudich and Miller, 1990). This approach and the a-posteriori analysis of the explored
147 ensemble of models have been extensively tested and used in previous works (detailed
148 description of the method can be found for example in Piatanesi and Lorito, 2007; Lorito et
149 al., 2011; Romano et al., 2014 and references therein).

150 We make some a-priori assumptions on ranges for slip and rake: for each subfault the slip
151 can vary from 0 to 15 m at 0.5 m steps, whereas the rake can vary from 40° to 100° at 5°
152 steps on 3 large blocks (see Fig. S1). Furthermore, we assume a circular rupture front that
153 propagates with a rupture velocity of 1.5 km/s (Lay et al., 2013).

154 In each inversion we retrieve the best fitting slip distribution model, the average model
155 obtained by the ensemble of models that fits the data fairly well, and the standard deviations
156 for each inferred model parameter (Table S3).

157

158 **3.1 Checkerboard resolution test**

159 We evaluate the resolving power of the inversion setup (i.e., fault parameterization and
160 instrumental azimuthal coverage) by means of a synthetic test. In particular, we attempt to
161 reproduce a slip distribution assuming a target checkerboard pattern with slip values of 0 and
162 10 m on alternating subfaults (Fig. 3a). In addition, we set the target rake angle on the
163 easternmost, middle, and westernmost blocks equal to 90° , 70° , and 50° , respectively. We
164 invert the synthetic tsunami waveforms resulting from the target slip pattern by following
165 the same inversion procedure described above. Synthetic tsunami waveforms are corrupted
166 by adding Gaussian random noise with a variance that is the 10% of the clean waveform
167 amplitude variance. The average model for slip distribution (Fig. 3b) reproduces very well
168 the checkerboard target (Fig. 3a). We observe that the maximum differences between the

169 target and the retrieved slip models are smaller than 1 m on average (absolute value), with a
170 maximum discrepancy of ~ 2.5 m along the deepest subfaults. The chosen inversion setup is
171 also well calibrated to recover the target slip direction (i.e., the rake angle) on the fault
172 plane, and the comparison between the synthetic and predicted tsunami waveforms shows an
173 excellent agreement (Fig. S3). We point out that such a checkerboard test only allows the
174 analysis of the resolution that is granted in principle by the inversion setup (model geometry,
175 station distribution). Possible epistemic uncertainty that is inherent in the numeric tsunami
176 model and/or due to the inaccuracy of the bathymetric model cannot be quantified in this
177 way. Accordingly, the uncertainty associated to the average slip model (Table S3) is
178 addressed through the analysis of the model ensemble, as discussed in the previous section.

179
180

181 **4 Source of the 2013 Santa Cruz Islands tsunami**

182 We use the same inversion scheme, fault parameterization, and set of DART buoys and tide
183 gauges data used for the checkerboard test to retrieve the coseismic tsunami source of the
184 Santa Cruz Islands earthquake. The coseismic rupture pattern (average model, Table S3)
185 shows a main patch of slip (Fig. 4), located SE from the hypocenter, centred around
186 $\sim 165.5^\circ\text{E}$ $\sim 11^\circ\text{S}$, and featuring a maximum slip value of ~ 11 m at a depth of ~ 25 km. The
187 coseismic rupture reaches the shallowest portion of the subduction interface and it spreads
188 along strike in NW direction with maximum slip values of ~ 6 m. The dislocation model
189 resulting from the inversion shows a second smaller patch of slip located NW from the
190 hypocenter and centred at a depth of ~ 29 km around $\sim 165^\circ\text{E}$ $\sim 10.5^\circ\text{S}$ (Fig. 4). This patch
191 has a maximum slip of ~ 4 m. We found an average rake angle of $\sim 85^\circ$ in the easternmost
192 part of the fault that is consistent with the relative convergence of the Australia and Pacific
193 plates in this portion of the megathrust. On the other hand, the remaining part of the fault
194 plane to the west is characterized by a slip angle lower than 50° . Hence, the dislocation there
195 highlights a relevant strike-slip component, according with the change of the tectonic regime
196 in this region, from purely thrust to left-lateral, as also shown by the regional seismicity.
197 Figure 5 shows an overall good agreement between observed and predicted tsunami
198 waveforms. During the inversion we applied a time shift (+2 min) to the Green's functions
199 of Lata Wharf tide gauge due to the systematic anticipation of the predicted tsunami
200 waveform with respect to the observed signal. This systematic difference between observed
201 and predicted data is likely due to the relatively low accuracy of the nearshore bathymetry
202 around this station. We also proved the validity of the linearity assumption at the coastal tide

203 gauges. The tsunami signals predicted with the time-shifted and linearly combined Green's
204 functions are compared to the tsunami signals produced with a single forward run forced by
205 the average slip model (Figure S4). This is in fair agreement with recent results of Yue et al.
206 (2015).

207 The total seismic moment associated to the slip distribution resulting from the inversion,
208 using a shear modulus equal to 30 GPa, is $M_0 = 1.033 \times 10^{21}$ Nm, that is equivalent to a
209 moment magnitude $M_w = 8.0$ and in agreement with the estimations obtained from previous
210 studies.

211

212

213 **5 Discussion**

214 **5.1 Comparison with previous Santa Cruz Islands earthquake source**

215 **models**

216 In principle, teleseismic data well constrain the earthquake seismic moment and the seismic
217 rupture history, and, compared to tsunami data, they are less sensitive to the spatial details of
218 the slip distribution (e.g. Yue, 2014; Gusman et al., 2015). Moreover, adopting different
219 fault geometries (and hypocenter) may result in different earthquake slip distributions (e.g.
220 Baba et al., 2009; Hayes et al., 2014b).

221 The comparison among the present model, LA13, and HA14 shows some differences in
222 terms of tsunami source that may be ascribed to the different data and fault model used in
223 the inversions.

224 The slip model in this study, LA13, and HA14 models have been obtained using three
225 different fault geometries (Fig. 6). Indeed, both LA13 and HA14 use a planar fault, whereas
226 we adopt a 3D fault surface honouring the subduction zone interface. In addition, the fault in
227 LA13 is overall shallower with respect to that in HA14, and LA13 also assumes a shallower
228 hypocenter (~ 13 km, whereas it is ~ 29 km in HA14, compare Figs. 6b,d).

229 As shown in Lay et al. (2013), the slip distributions of the Santa Cruz Islands earthquake
230 obtained by using only teleseismic data, adopting a hypocenter deeper than 15 km, and an
231 overall deeper fault plane result in an under-prediction of tsunami observations at DART
232 buoys. For this reason, Lay et al. (2013) prefer, among teleseismic solutions, the one
233 obtained by imposing a shallower hypocenter. Since the model in this study and LA13
234 explain tsunami data to a similar extent, then the main differences between the two may be
235 ascribed either to differences in the adopted fault geometry, or to poor resolving power of
236 tsunami data themselves, which would lead to non uniqueness of the solution. According to

237 our synthetic test, the latter does not seem to be the case, at least as regards the most
238 tsunamigenic part of the source, that is the one with a dominant dip slip component in LA13
239 model. Besides this, we also may argue that the HA14 source, which shows a deeper slip
240 centroid than LA13 (and lower peak slip of about 4 m, Fig. 6a), should result less
241 tsunamigenic with respect to LA13 (peak slip > 10 m, Fig. 6c), and then likely
242 underestimate tsunami observations.

243 The centroid of the main asperity individuated in the present study is shifted SE with respect
244 to the main one of HA14 and it features quite larger slip (Fig. 6a). Conversely, it features
245 comparable peak slip values to the shallower patch in LA13 (Fig. 6c), but it is nearer to the
246 Nendo Island, as the two are only partially overlapped.

247 We also observe that the rake angle associated to our model is pretty consistent with the
248 relative convergence direction between Australia and Pacific plates. In particular, the slip
249 direction has behaviour close to a thrust-like motion (rake $\sim 85^\circ$) in the SE part of the fault
250 just nearby the northern-end of Vanuatu subduction zone; then the slip direction becomes
251 progressively more oblique highlighting a significant left-lateral component that is in
252 agreement with the kinematics (DeMets et al., 2010) and the seismicity of the NW segment
253 of the subduction (Fig. 1). On the other hand, we observe an opposite behaviour of the rake
254 angle in LA13; indeed, the southeastern shallower patch in LA13 has a slip direction with a
255 strong oblique component, whereas the northern deeper patch shows a thrust-like fault
256 motion. Thus, the main tsunamigenic patch in LA13 is located around the hypocenter,
257 whereas in the present study it is located in front of the Nendo Island, very close to the area
258 where the maximum tsunami wave heights have been observed (Fig. 1; Fritz et al., 2014;
259 NOAA/NGDC, http://www.ngdc.noaa.gov/hazard/tsu_db.shtml). Hence, as a likely less
260 tsunamigenic patch is involved, these differences may be due to a combination of the effects
261 of different resolving power of the data used and of different fault geometry.

262 In a further analysis, we observe that $\sim 97\%$ of the total seismic moment in our model is
263 released within 75 s from the nucleation. In particular, $\sim 60\%$ of the moment release occurs
264 between 15 and 45 s, as this time window includes most of the main asperity and the peak
265 slip area (Fig. 4). Thus, at least qualitatively, the moment rate we derive by combining the
266 retrieved slip distribution and the imposed rupture velocity is in agreement with the moment
267 rate function resulting from teleseismic inversions.

268
269 **5.2 Seismic rupture propagation SE from the hypocenter**

270 The distribution of the early aftershocks (in the first 48h after the mainshock,
271 <http://earthquake.usgs.gov/earthquakes/?source=sitenav>), shows a lack of significant
272 seismic events occurring at the subduction interface, a feature that might be indicative of a
273 complete stress drop associated to the main 6 February event. On the other hand, a large
274 number of seismic events have been observed mainly in the upper crust of the Pacific plate
275 and in the eastern edge of the Australia plate oceanic crust (Fig. 4). In particular, the largest
276 one in the Pacific plate (M_w 7+) occurred North of Nendo Island with a strike-slip right-
277 lateral mechanism (Fig. 1) that is consistent with the kinematics of the coseismic slip
278 (HA14). In addition, a cluster of shallow right-lateral aftershocks occurred SE from the
279 mainshock epicenter (magenta ellipse in Fig. 4). In their study, HA14 propose that
280 occurrence of these strike-slip earthquakes is caused by the block-like motion behaviour of
281 the Pacific upper plate. However, they also argue that the Coulomb stress change
282 distribution resulting from the HA14 coseismic model would promote events with left-
283 lateral behaviour, whereas significant additional slip located SE from the hypocenter would
284 promote the observed right-lateral aftershocks. They conclude that such slip (see magenta
285 shaded ellipse in Fig. 6a), as not observed in HA14, then should be aseismic, should occur at
286 the megathrust interface, and, in agreement with the Coulomb stress transfer estimation,
287 should release a seismic moment of $M_0 = 3.1 \times 10^{20}$ Nm. Thus, the total (coseismic +
288 aseismic) seismic moment released along the southeastern portion of the fault results to be
289 $M_0 = 3.9 \times 10^{20}$ Nm. Noteworthy, our slip model is partially overlapped with the aseismic slip
290 area argued by HA14; in particular, we observe larger slip values, up to 9 m confined in a
291 smaller area, versus an average of 2 m of slip on a larger portion of the megathrust (Fig. 6a).
292 The seismic moment associated to this portion of slip distribution in our model is $M_0 =$
293 4.08×10^{20} Nm, that is quite compatible with the estimation by HA14.

294 The location of the coseismic tsunami source that we found here is not in contradiction with
295 the images of the rupture propagation resulting from back-projection analyses (IRIS,
296 <http://ds.iris.edu/spud/backprojection/1065729>). Indeed, all of these analyses, while showing
297 different features depending on the seismic network employed, highlight a possible rupture
298 propagation south-eastward from the hypocenter, shown as well by the slip models obtained
299 using tsunami data (this study and LA13). Furthermore, on one hand in the back-projection
300 analyses the surface projection of the radiated energy shows coherent high-frequency
301 radiation along a portion of the megathrust corresponding to the seismogenic layer; on the
302 other hand, the coherence of seismic high-frequency radiation appears to degrade south-
303 eastward at shallower depths. This feature, along with the slip propagation up to the trench

304 (a zone likely rich of sediments) and the relatively low rupture velocity (1.5 km/s, LA13)
305 suggests that part of the seismic rupture SE of Nendo Island may have been characterized by
306 slow slip, as indicated by LA13. Therefore, we cannot rule out that this portion of the
307 megathrust, at least partially, may have slipped coseismically triggering the right-lateral
308 strike-slip aftershocks.

309

310

311 **6 Conclusion**

312 We retrieved the coseismic tsunami source of the 2013 Santa Cruz Islands earthquake by
313 inverting tsunami observations recorded in the Pacific Ocean by several DART buoys and
314 tide gauges. We also computed the Green's functions using a 3D fault model honouring the
315 geometrical complexities of the subduction interface. The retrieved coseismic tsunami
316 source is mainly located SE from the hypocenter, with maximum slip value of ~ 11 m and
317 with the coseismic rupture reaching the shallow part of the megathrust with slip amplitudes
318 up to 6 m. The seismic moment resulting from our coseismic slip model is equivalent to an
319 M_w 8.0 moment magnitude, in agreement with previous studies. The spatial pattern of the
320 tsunami source is in agreement with the Australia and Pacific plates convergence direction
321 that becomes progressively more oblique in the NW segment, and the slip distribution well
322 reproduces the tsunami data. However, our model, compared with previously published
323 models, features some differences in terms of tsunamigenesis and pattern of coseismic slip,
324 that we have discussed in relation to the different resolving power of the data used and on
325 the different fault geometry adopted. A common feature to all the models is the presence of
326 slip SE from the hypocentre, which we argue to have occurred during the coseismic stage,
327 possibly with a slow slip component, rather than being aseismic as previously suggested.

328 **Author contributions**

329 F.R. was involved in all of the phases of this study. I.M. built the 3D fault geometry,
330 processed tsunami data, and contributed to write the paper. S.L. and A.P. contributed to
331 design the experiment, to discuss and interpret the results and writing the paper. All authors
332 reviewed the final manuscript.

333

334

335 **Acknowledgments**

336 This work is partially funded by project ASTARTE - Assessment, Strategy And Risk
337 Reduction for Tsunamis in Europe - FP7-ENV2013 6.4-3, Grant 603839, and by the Italian
338 flagship project RITMARE. Some of the figures in this work were drawn using GMT
339 software (Wessel and Smith, 1995) and Matlab (<http://www.mathworks.it/products/matlab/>).

340

341 **References**

- 342 Aki, K.: Characterization of barriers on an earthquake fault, *J. Geophys. Res.*, 84,
343 6140-6148, 1979.
- 344
- 345 Baba, T., Cummins, P. R., Thio, H. K., and Tsushima, H.: Validation and Joint Inversion of
346 Teleseismic Waveforms for Earthquake Source Models Using Deep Ocean Bottom Pressure
347 records: A Case Study of the 2006 Kuril Megathrust Earthquake, *Pure Appl. Geophys.*, 166,
348 55-76, doi:10.1007/s00024-008-0438-1, 2009.
- 349
- 350 Barbosa, S. M., Fernandes, M. J., and Silva, M. E.: Nonlinear sea level trends from
351 European tide gauge records, *Ann. Geophys.*, 22, 1465–1472, doi:10.5194/angeo-22-1465-
352 2004, 2004.
- 353
- 354 Bird, P.: An updated digital model of plate boundaries, *Geochem. Geophys. Geosyst.*, 4,
355 1027, doi:10.1029/2001GC000252, 2003.
- 356
- 357 DeMets, C., Gordon, R. G., and Argus, D. F.: Geologically current plate motions, *Geophys.*
358 *J. Int.* 181, 1–80, doi:10.1111/j.1365-246X.2009.04491.x, 2010.
- 359
- 360 Engdahl, E.R., van der Hilst, R., and Buland, R.: Global teleseismic earthquake relocation
361 with improved travel times and procedures for depth determination, *Bull. Seism. Soc. Am.*,
362 88, 722-743, 1998.
- 363
- 364 Fritz, H. M., Papantoniou, A., Biukoto, L., Gilly, A., and Wei, Y.: The Solomon Islands
365 Tsunami of 6 February 2013 in the Santa Cruz Islands: Field Survey and Modeling, EGU
366 General Assembly 2014, held 27 April - 2 May, in Vienna, Austria, id.15777, 2014.
- 367
- 368 Gusman, A. R., Murotani, S., Satake, K., Heidarzadeh, M., Gunawan, E., Watada, S., and
369 Schurr, B.: Fault slip distribution of the 2014 Iquique, Chile, earthquake estimated from
370 ocean-wide tsunami waveforms and GPS data, *Geophys. Res. Lett.*, 42,
371 doi:10.1002/2014GL062604, 2015.
- 372

373 Hayes, G.P., Wald, D.J., and Johnson, R.L.: Slab1.0: A three-dimensional model of global
374 subduction zone geometries, *J. Geophys. Res.* 117, B01302, doi:10.1029/2011JB008524,
375 2012.

376

377 Hayes, G.P., Furlong, K.P., Benz, H.M., and Herman, H.W.: Triggered aseismic slip
378 adjacent to the 6 February 2013 Mw8.0 Santa Cruz Islands megathrust earthquake, *Earth*
379 *Planet. Sci. Lett.* 388, 265-272, doi: 10.1016/j.epsl.2013.11.010, 2014a.

380

381 Hayes, G.P., Herman, M. W., Banhart, W. D., Furlong, K. P., Riquelme, S., Benz, H.M.,
382 Bergman, E., Barrientos, S., Earle, P. S., and Samsonov, S.: Continuing megathrust
383 earthquake potential in Chile after the 2014 Iquique earthquake, *Nature* 512, 295–298,
384 doi:10.1038/nature13677, 2014b.

385

386 Lay, T., Ye, L., Kanamori, H., Yamazaki, Y., Cheung, K.F., and Ammon, C.J.: The
387 February 6, 2013 Mw 8.0 Santa Cruz Islands earthquake and tsunami, *Tectonophysics*, 608,
388 1109-1121, doi:10.1016/j.tecto.2013.07.001, 2013.

389

390 Lorito, S., Romano, F., Atzori, S., Tong, X., Avallone, A., McCloskey, J., Cocco, M.,
391 Boschi, E., and Piatanesi, A.: Limited overlap between the seismic gap and coseismic slip of
392 the great 2010 Chile earthquake, *Nature Geosci.*, 4(3), 173-177, doi:10.1038/NGEO1073,
393 2011.

394

395 Meade, B. J.: Algorithms for the calculation of exact displacements, strains, and stresses for
396 triangular dislocation elements in a uniform elastic half space, *Comput. Geosci.* 33, 1064-
397 1075, doi:10.1016/j.cageo.2006.12.003, 2007.

398

399 Piatanesi, A., and Lorito, S.: Rupture process of the 2004 Sumatra-Andaman earthquake
400 from tsunami waveform inversion, *Bull. Seismol. Soc. Am.*, 97(1), 223-231,
401 doi:10.1785/0120050627, 2007.

402

403 Romano, F., Piatanesi A., Lorito, S., D'Agostino, N., Hirata, K., Atzori, S., Yamazaki, Y.,
404 and Cocco, M.: Clues from joint inversion of tsunami and geodetic data of the 2011 Tohoku-
405 oki earthquake, *Sci. Rep.* 2, 385; DOI:10.1038/srep00385, 2012.

406

407 Romano, F., Trasatti, E., Lorito, S., Piromallo, C., Piatanesi, A., Ito, Y., Zhao, D., Hirata, K.,
408 Lanucara, P., and Cocco, M.: Structural control on the Tohoku earthquake rupture process
409 investigated by 3D FEM, tsunami and geodetic data, *Sci. Rep.*, 4, 5631,
410 doi:10.1038/srep05631, 2014.

411

412 Rothman, D.: Automatic estimation of large residual statics corrections, *Geophysics* 51,
413 332–346, doi:10.1190/1.1442092, 1986.

414

415 Spudich, P., and Miller, D. P.: Seismic site effects and the spatial interpolation of earthquake
416 seismograms: results using aftershocks of the 1986 North Palm Springs, California,
417 earthquake, *Bull. Seismol. Soc. Am.* 80, 6, 1504–1532, 1990.

418

419 Tanioka, Y., and Satake, K.: Tsunami generation by horizontal displacement of ocean
420 bottom, *Geophys. Res. Lett.* 23, 8, 861-864, doi:10.1029/96GL00736, 1996.

421

422 Wessel, P., and Smith, W. H. F.: New version of the Generic Mapping Tools released, *Eos*
423 *Trans. AGU*, 76, 329, doi:10.1029/95EO00198, 1995.

424

425 Yamazaki, Y., Kowalik, Z., and Cheung, K. F.: Depth-integrated, non-hydrostatic model for
426 wave breaking, *Int. J. Numer. Meth. Fluids*, 61, 473–497, doi:10.1002/flid.1952, 2009.

427

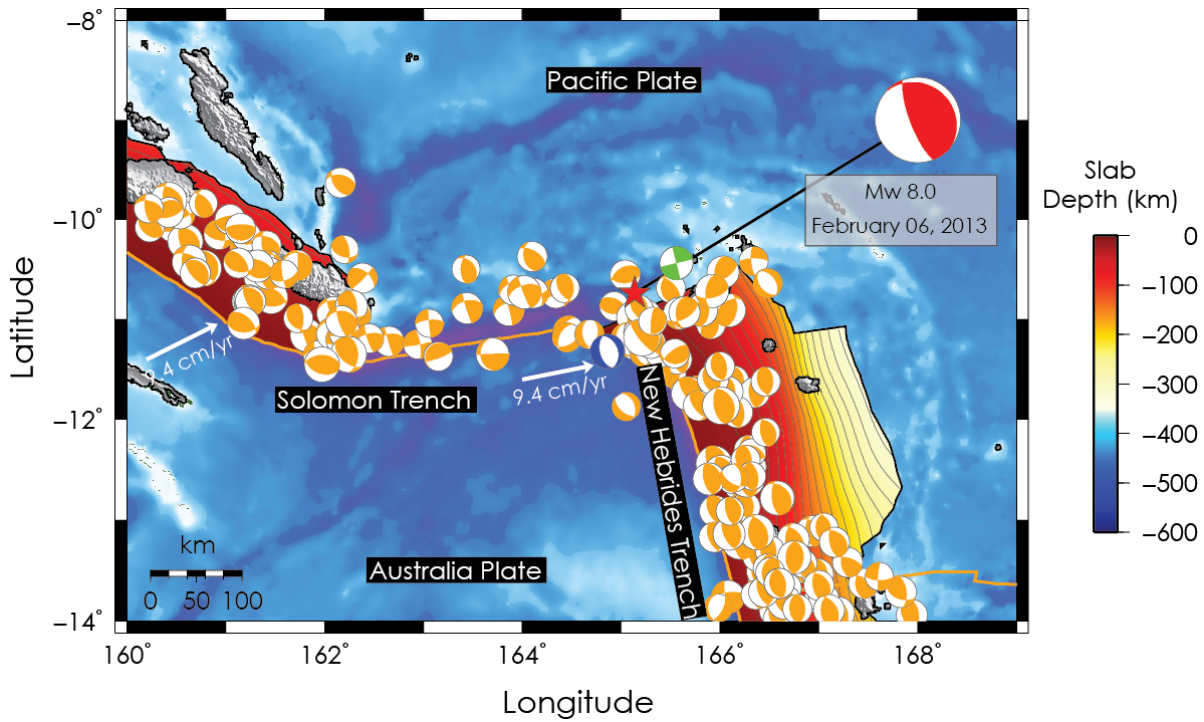
428 Yamazaki, Y., Cheung, K. F., and Kowalik, Z.: Depth-integrated, non-hydrostatic model
429 with grid nesting for tsunami generation, propagation, and run-up, *Int. J. Numer. Meth.*
430 *Fluids*, 67, 2081–2107, doi:10.1002/flid.2485, 2011.

431

432 Yue, H: Toward resolving stable high-resolution kinematic rupture models of large
433 earthquakes by joint inversion of seismic, geodetic and tsunami observations, PhD Thesis,
434 2014.

435

436 Yue, H., Lay, T., Li, L., Yamazaki, Y., Cheung, K.F., Rivera, L., Hill, E.M., Sieh, K.,
437 Kongko, W., and Muhari, A.: Validation of linearity assumptions for using tsunami
438 waveforms in joint inversion of kinematic rupture models: Application to the 2010
439 Mentawai Mw 7.8 tsunami earthquake, *J. Geophys. Res. Solid Earth*, 120, 1728-1747,
440 doi:10.1002/2014JB011721, 2015.

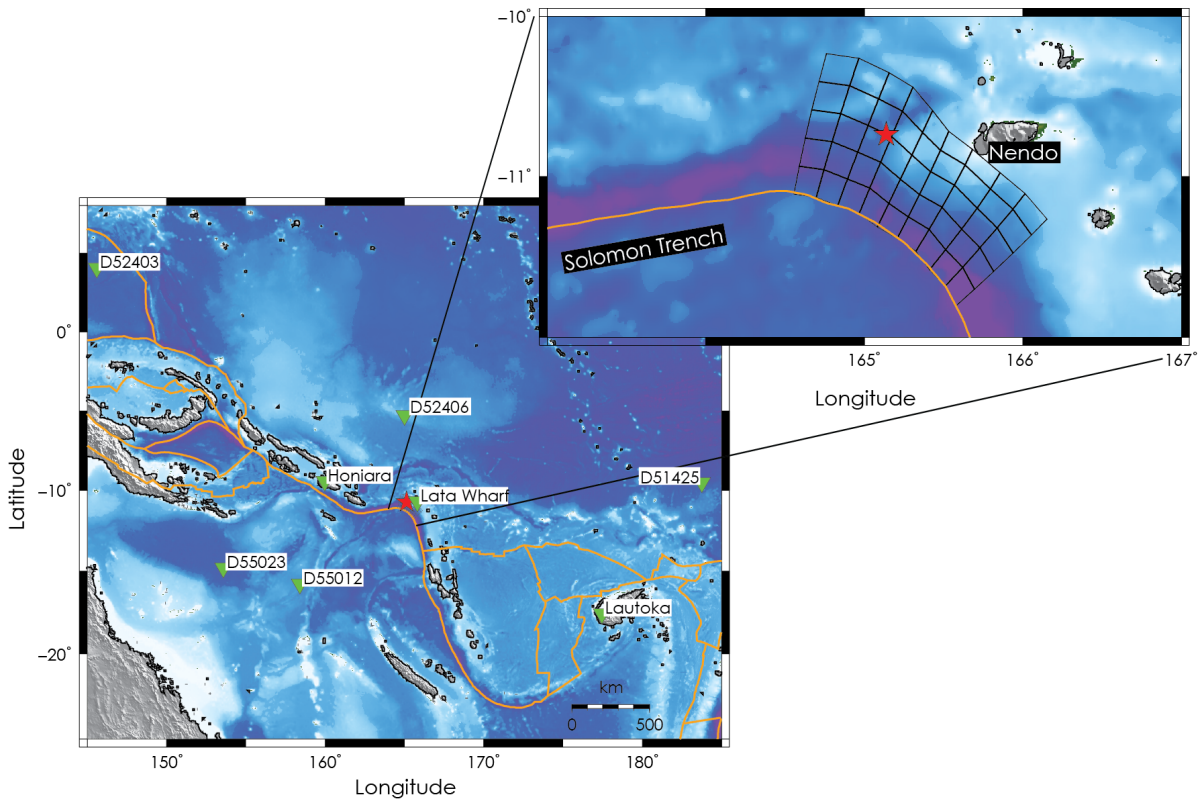


441

442

443 **Figure 1 – Location map of the 2013 Santa Cruz Islands earthquake.** Red star and red
 444 beach ball indicate epicenter and focal mechanism of the mainshock, respectively. Green
 445 and blue beach balls indicate the focal mechanisms of the largest strike-slip (M_w 7.0) and
 446 normal (M_w 7.1) aftershocks occurred few hours after the mainshock. Orange beach balls
 447 indicate the regional historical seismicity (since 1976 to present, GCMT catalogue,
 448 <http://www.globalcmt.org/CMTsearch.html>) and the corresponding focal mechanisms for
 449 earthquake magnitude 6+. White arrows indicate the convergence direction of the Australia
 450 Plate.

451

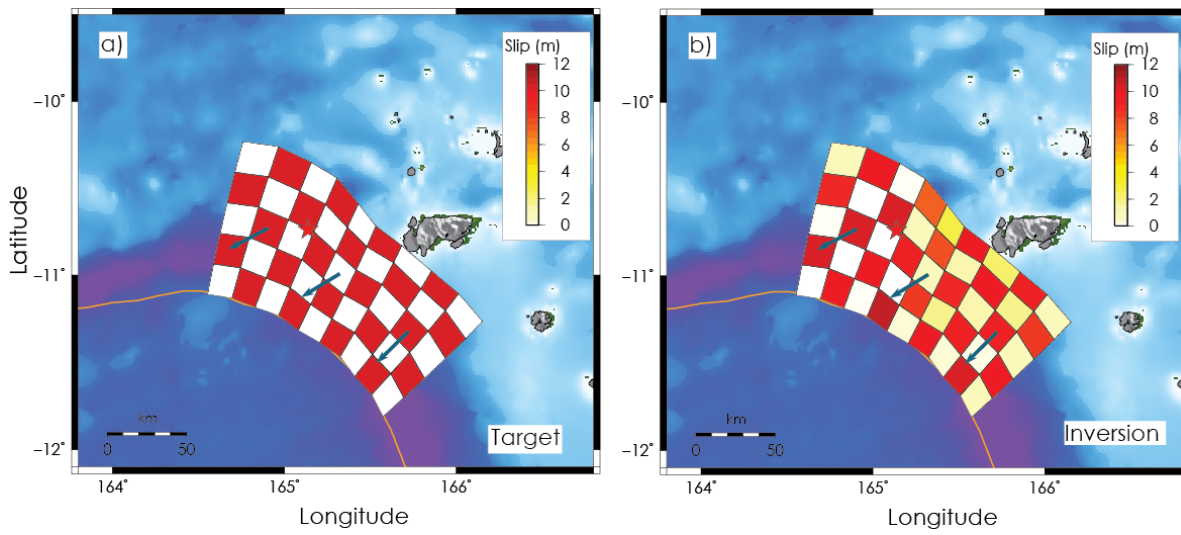


452

453

454 **Figure 2 – Data and fault model.** Green triangles indicate DART buoys and tide gauges
 455 used in this study. The top-right panel is a close-up view of the fault model adopted. Red
 456 star indicates the Santa Cruz Islands earthquake epicenter.

457

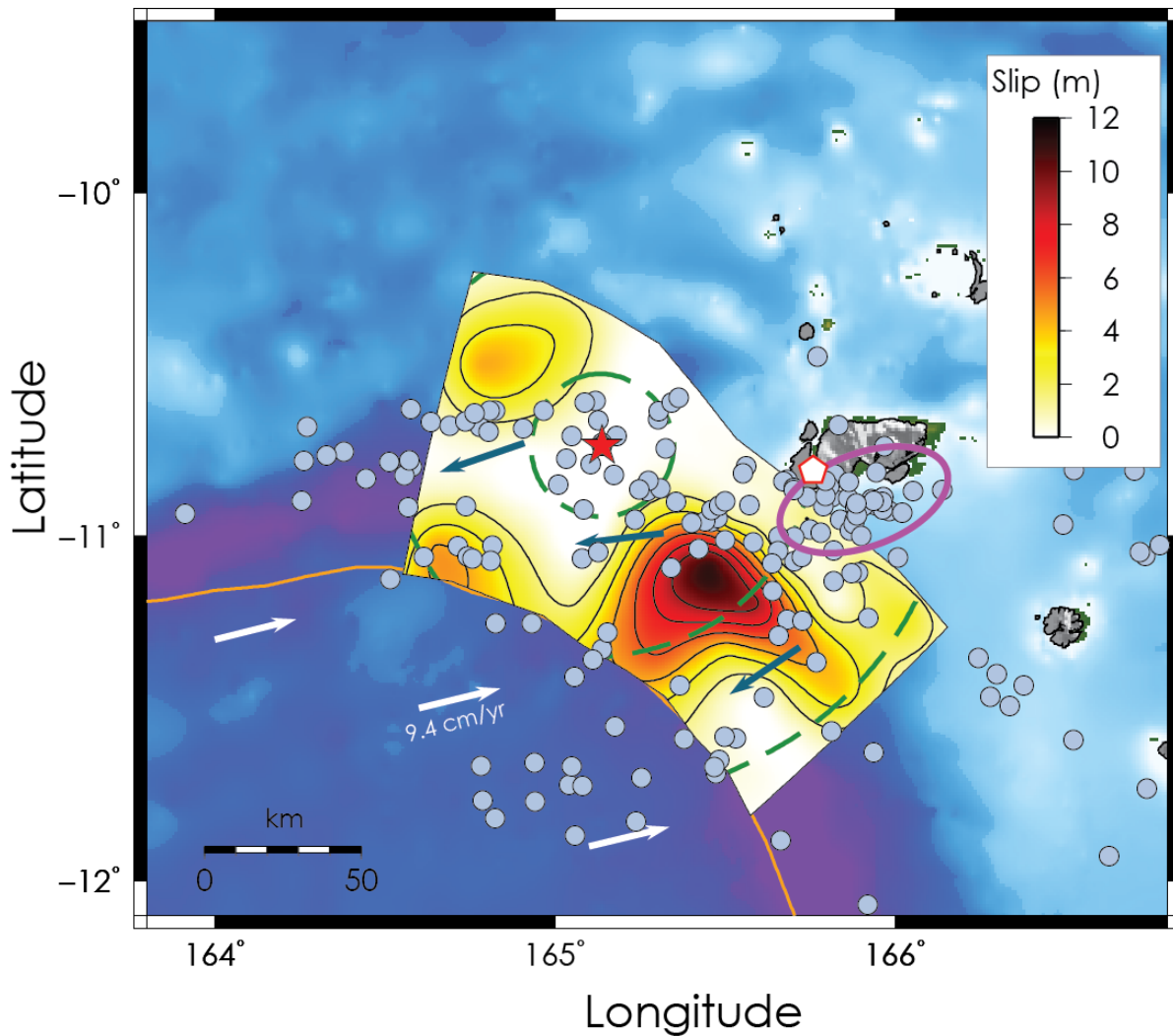


458

459

460 **Figure 3 – Resolution test.** a) Target slip and rake (blue arrows) pattern; b) slip model

461 obtained inverting tsunami data.

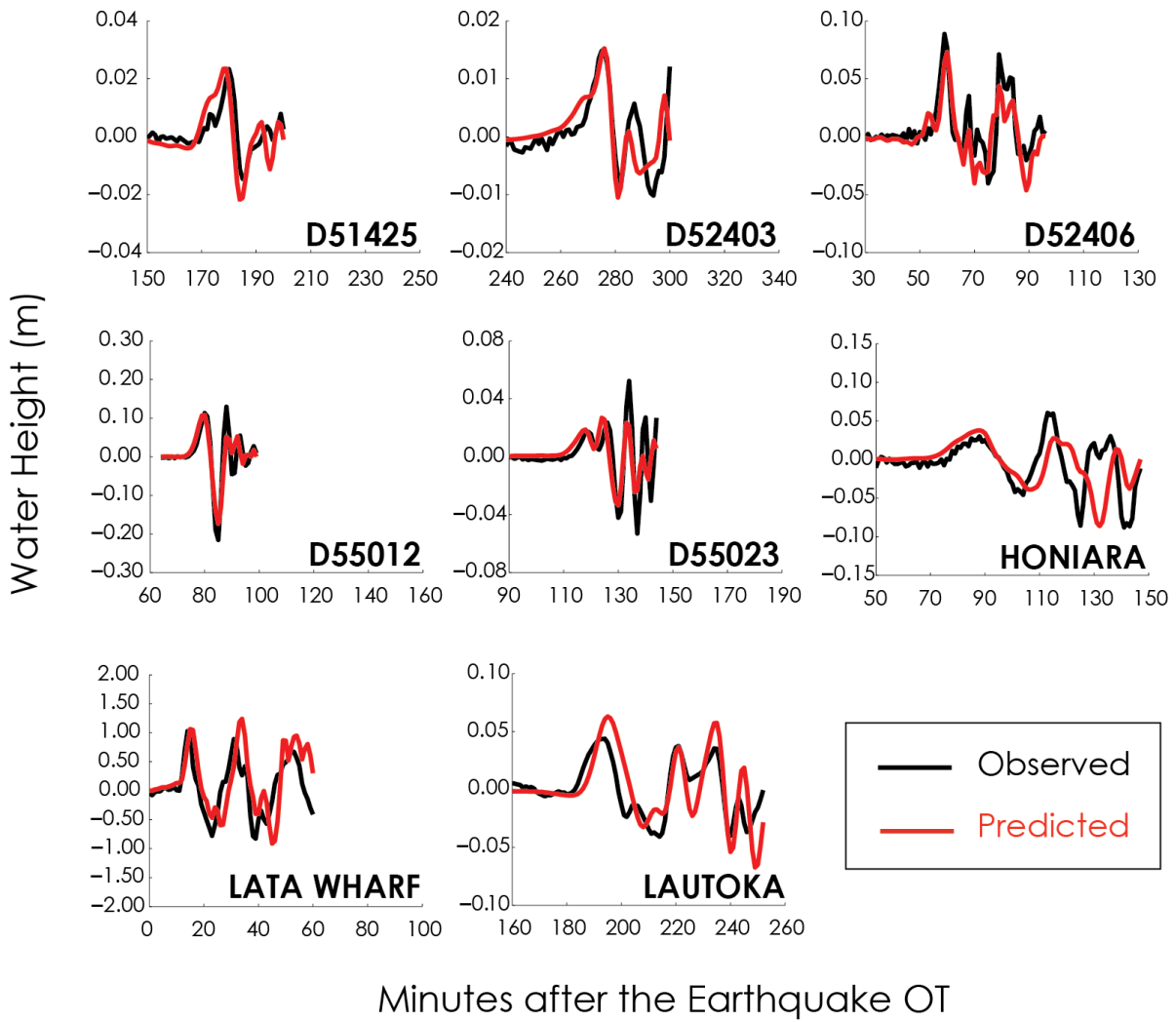


462

463

464 **Figure 4 – Coseismic tsunami source of the 2013 Santa Cruz Islands earthquake.** Slip
 465 model is contoured (black solid line) in 1.5 m intervals. Blue arrows indicate the rake. White
 466 arrows indicate the convergence direction of the Australian Plate. Cyan dots represent the
 467 early aftershocks (occurred within 48 hours after the mainshock, NEIC catalogue). Magenta
 468 ellipse approximately indicates the cluster of right-lateral strike-slip aftershock events.
 469 White pentagon indicates the area where the maximum tsunami wave heights have been
 470 observed (Fritz et al., 2014; NOAA/NGDC,
 471 http://www.ngdc.noaa.gov/hazard/tsu_db.shtml). Green dashed circles represent the rupture
 472 front expansion (rupture velocity 1.5 km/s) at 15, 45, and 75 s.

473

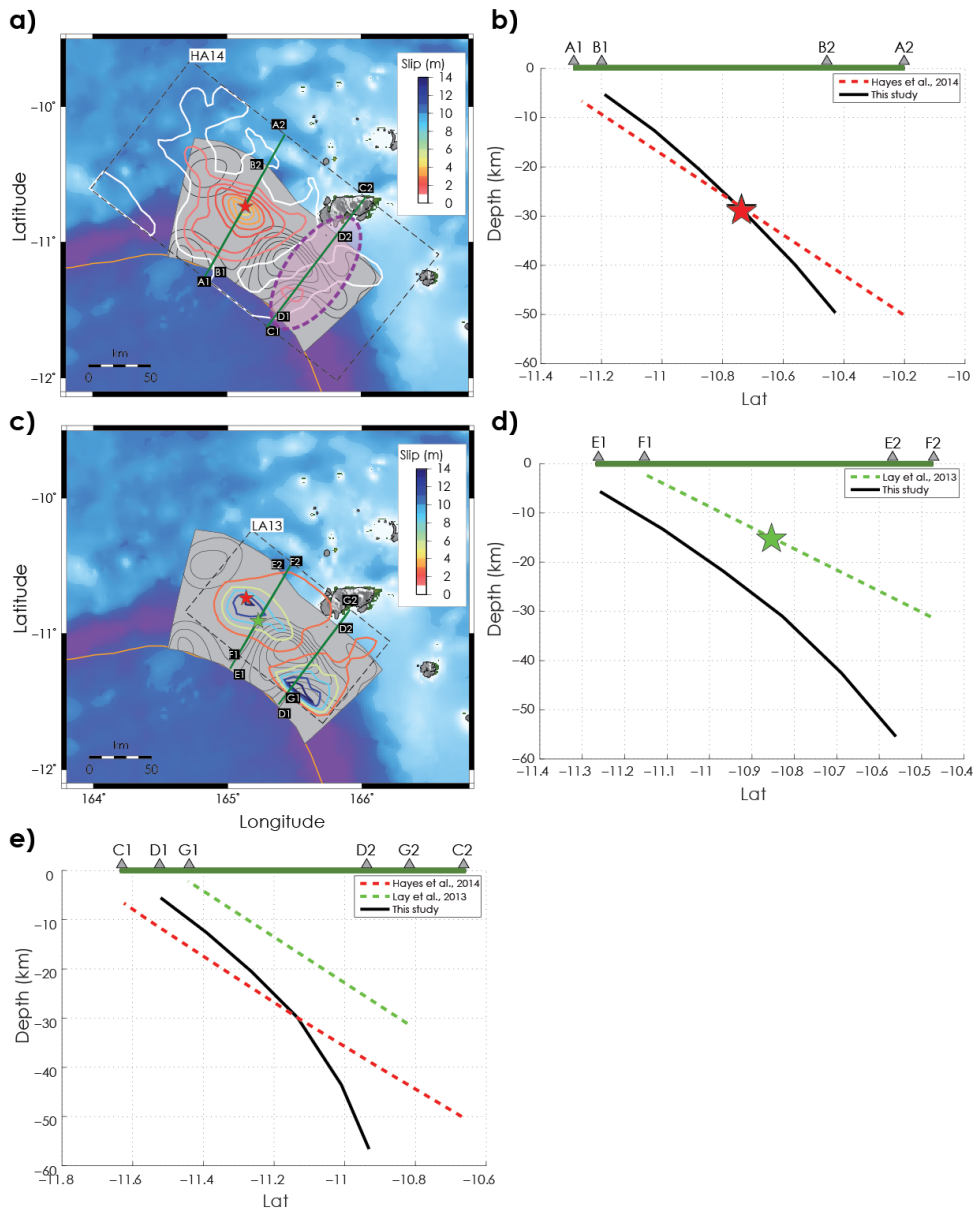


474

475

476 **Figure 5 – Data fit.** Comparison between observed (black) and predicted (red) tsunami data.

477



478
479

480 **Figure 6 – Comparison with other source models.** a) HA14 model (coloured solid lines at
481 0.5 m intervals); magenta ellipse approximately represents the aseismic slip area
482 hypothesized in HA14; black solid lines as in Figure 4; green solid lines represent the
483 surface projections of the depth profiles along the HA14 fault model and that one adopted in
484 this study. b) Depth profiles along the HA14 fault model (red) and that one adopted in this
485 study (black) crossing the hypocenter used in HA14 (red star) and in this study (black star);
486 notice that the two hypocenters are almost coincident. c) LA13 model (coloured solid lines
487 at 2.8 m intervals); black solid lines as in Figure 4; green solid lines represent the surface
488 projections of the depth profiles along the LA13 fault model and that one adopted in this
489 study. d) Depth profiles along the LA13 fault model (green) and that one adopted in this
490 study (black) crossing the hypocenter used in LA13 (green star).

491 LA13 and HA14 fault models and that one adopted in this study crossing the aseismic slip
492 area hypothesized in HA14.